NUMERICAL SIMULATION OF THE DUCTED PROPELLER AND APPLICATION TO A SEMI-SUBMERGED VEHICLE

Jin Zou
Harbin Engineering University, China
Guoge Tan
Harbin Engineering University, China
Hanbing Sun
Harbin Engineering University, China
Jie Xu
Chongqing Changan Automobile Co., Ltd., China
Yongkang Hou
Harbin Engineering University, China

ABSTRACT

The self-propulsion test of underwater vehicles is the key technique for predicting and evaluating the navigation performance of these submersibles. In this study, the numerical simulation of a standard propeller JD7704+Ka4-70 is first presented and the results are compared with experiments to validate the numerical approaches. The reason why the propulsion efficiency of the ducted propeller is higher than that of the conventional propeller is explored. Then, the paper proposes a series of numerical simulations conducted to test the performance of the ducted propeller designed according to the JD7704+Ka4-70 in order to match with the unmanned semi-submerged vehicle (USSV), and the propeller's open water characteristic curves are obtained. The results show a reasonable agreement with the regression analysis. Afterwards, the numerical simulations focus on a self-propulsion test of the USSV with the designed ducted propeller and the self-propulsion point is obtained. The streamlines through the hull as well as the ducted propellers are clearly obtained, together with the velocity distributions of the propeller plane. The results vividly demonstrate the hydrodynamic performance of the USSV with the designed propellers. In this paper, all the CFD simulations are based on the numerical software, Star-CCM+, and use the Reynolds-averaged Navier−Stokes (RANS) equations with the shear stress transport (SST) k-omega turbulence model.

Keywords: open water test, self-propulsion test, ducted propeller, unmanned semi-submerged vehicle

INTRODUCTION

It is well known that propeller performance and efficiency play an essential role in marine vessels, especially in underwater vehicles. One of the main goals of underwater vehicle designers and researchers is to estimate satisfactorily the resistance and self-propulsion characteristics for different velocities [1]. Therefore, the analysis of the interaction between the propeller and the hull by a self-propulsion test is the key technology for evaluating the navigation performance of vessels. For this purpose, computational fluid dynamics (CFD), which has been widely used for simulating the flow around ships, can provide a more effective and efficient way to validate new propeller designs compared with experimental fluid dynamics (EFD).

The forces acting on the propeller have been studied and experimentally tested for over 70 years [2]. The self-propulsion experiment includes a propeller open water test, a model resistance test and a self-propulsion test. Nowadays, research on self-propulsion testing focuses mainly on the study of surface ships. For example, Yang et al. studied the flow field of a KCS container ship and a KVLCC2 tanker sailing with a propeller and rudder [3]. Tahara et al. carried out steady flow analyses for the KCS model using two different RANS solvers [4]. The numerical results of the self-propulsion test showed a good agreement with the available experimental

results. Cheng et al. presented the CFD results of a propeller open water test, model resistance test and self-propulsion test in their paper, which has a certain reference significance in the field of ship design and propeller performance evaluation [5]. Wu et al. analysed the flow around a KCS container ship in the self-propulsion test, based on the volume force method [6]. They calculated the position of the self-propulsion point in two conditions, with and without the rudder, by replacing the role of the propeller by applying thrust and torque directly to the grids of the propeller's active area. Their work verified the reliability of the volume force method. In the research by Carrica et al., they presented a method for calculating the self-propulsion of three different ships, namely the KVLCC1, the ONR Tumblehome and the KCS. The method was based on controlling the propeller's rotational speed to find the self-propulsion point, and the computational time could be reduced significantly [7]. Abbas et al. presented a hybrid method to compute the propeller forces of the ship [8]. In their work, a hybrid URANS-LES model was used to calculate the unsteady loadings on propellers of the KVLCC2 tanker model. The numerical results were compared with different empirical estimations and showed that the hybrid method overestimated the thrust loading. Ponkratov et al. focused on full-scale CFD simulations for self-propulsion analyses [9]. The numerical simulations were carried out using the SST k-ω turbulence model. In their research, in order to get the final results quickly, a moving reference frame (MRF) was used at first, then a rigid body motion (RBM) was applied with a lower time step size to obtain the self-propulsion point.

The abovementioned articles are all about self-propulsion studies on surface ships; however, there is relatively little research in the field of submerged vehicles. For example, Yang et al. simulated the self-propulsion test of a submarine model with a front vane propeller [10]. In their research, the self-propulsion point was obtained and self-propulsion factors were estimated. In [11], self-propulsion tests of the well-known submarine model DARPA Suboff with propellers in the deep-dive state and near-surface state were simulated separately. A seven-bladed propeller model INSEAN E1619 was studied with the DARPA Suboff model by Chase et al. [12]. The results showed that the present approach is applicable for predicting the self-propulsion performance of submarines. Zhang et al. focused on a study about the interaction between the propeller and the submarine hull [13]. In their process of analysis, the free surface effects were taken into account and the numerical results showed a reasonable agreement with the experimental results. It was concluded that the free surface effects of a submerged vehicle have a significant impact on the total resistance.

However, in addition to the above articles, simulations focused on self-propulsion tests of unmanned semi-submerged vehicles (USSV) are rare. The USSV is a new type of vessel that differs from surface ships and underwater vehicles. When sailing, the hull of the USSV dives to a certain depth below the water surface to reduce the influence of winds and waves. The mast is exposed above the water surface and has the function of maintaining the attitude of the USSV. The GPS carried on the mast can realise real-time positioning, avoiding the need for the underwater vehicle to float to the water surface to correct its GPS positioning periodically, thereby reducing energy consumption. The hydrodynamic performance of the USSV is likewise different from surface ships and underwater vehicles. Therefore, studying the influence of the interaction between the hull of the USSV and the propeller is of great significance in order to improve the propulsion efficiency.

In this study, based on the CFD software Star-CCM+, using RANS equations with the SST k-omega turbulence model, a numerical simulation of the open water test of a standard propeller JD7704+Ka4-70 is first carried out. The reason why the propulsion efficiency of the ducted propeller is higher than that of the conventional propeller is explored. Then the CFD simulation of the ducted propeller, which is designed based on JD7704+Ka4-70 in order to match with the USSV, is performed and the characteristic curves of the propeller are obtained. Afterwards, the numerical simulation focuses on the self-propulsion test of the USSV with the designed propellers.

THEORETICAL FUNDAMENTALS

NUMERICAL SIMULATIONS OF PROPELLER ROTATIONAL MOTION

The software Star-CCM+ provides two methods for calculating rotational motion. They are moving reference frames and rigid body motion. The former is known as the multiple reference frame (MRF), the latter is called the sliding mesh (SM).

The MRF model is used for steady calculations to solve the implicit steady flow problem. When the fluid goes through the region, the domain should be divided into a rotation domain containing moving objects and a static domain of the external flow field. The rotation domain contains the motion body and the static domain is the outflow field, which is used to monitor the hydrodynamic performance. The physical quantities of the flow field are transmitted by setting an interface between the two domains. The interface is a pair of faces that exist in two different regions, and the shape of the interface differs as determined by factors such as the shape and size of the rotating object. Different mesh types can be used on each side of the interface, but the size and number of meshes on both sides should be of the same magnitude as far as possible, which is beneficial to the data transfer.

In the static domain, the flow characteristics can be obtained directly by solving the established motion equations in the geodetic coordinate system; in the rotation domain, a relative coordinate system having the same moving and rotational speed as the moving object is established in the region, so that the moving object is in a stationary state in the relative coordinate system but in a moving state in the geodetic coordinate system. As Fig. 1 shows below, it is moving

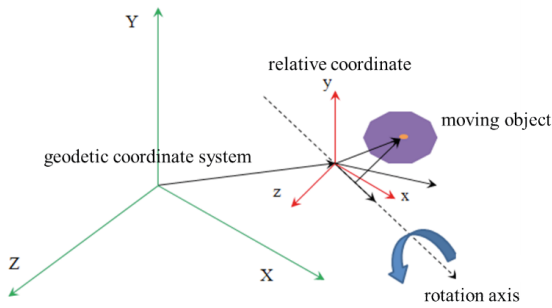in the geodetic coordinate system, but keeping static in the relative coordinate.

Fig. 1. Absolute frame and relative coordinate schematic

The SM model is used for non-stationary computation and solves the transient flow problem. The so-called slip grid ensures that when the calculation is carried out, the domain containing the moving object slides along the interface; this method can simulate the actual rotational motion, and at each new time step, the relative position of the grid on the interface is re-determined. The SM model is shown in Fig. 2 below.
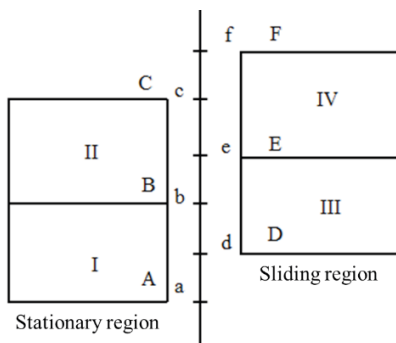
Fig. 2. Sliding mesh model

The two regions in Fig. 2 are area A-B-C and area D-E-F. At this moment, the interface area is d-b-e-c. For example, it is clear that the data in the area Unit I and Unit II is delivered through interface b-d and b-e into Unit III [14].

PROPELLER OPEN WATER TEST

The propeller model tested in the uniform water flow alone is called the propeller open water test. The propeller open water characteristics are determined by testing the propeller in free inflow with different propeller advance ratios $J = v_a/(nD)$. The propeller with the diameter D [m] is running at a constant rotation rate n [1/s], whereas the propeller advance velocity v_a [m/s] changes. The results are presented in normalised form as follows [15, 16]:

Thrust coefficient:

$$K_T = T/(\rho D^4 n^2) \qquad \text{(1)}$$

Torque coefficient:

$$K_Q = Q/(\rho D^5 n^2) \qquad \text{(2)}$$

Propeller efficiency:

$$\eta_0 = P_T/P_D \qquad \text{(3)}$$

where T [N] is the propeller thrust, Q [Nm] is the propeller torque, ρ is the density of the fluid, $P_T = T \cdot v_a$ [W] denotes the thrust power, $P_D = Q \cdot \omega'$ [W] denotes the delivered power and $\omega' = 2\pi n$ [rad/s] represents the circular frequency of propeller revolutions.

DETERMINATION OF SELF-PROPULSION POINT

The determination of the self-propulsion point is described as follows: the open water test of the ducted propeller carried on the USSV is performed first, and after the open water characteristic curves of the propeller are obtained, the numerical simulation of the "free surface-USSV-ducted propeller" as a whole will be carried out to obtain propeller hydrodynamic coefficients according to the resistance curves of the USSV at different speeds. The detailed flow chart is shown in Fig. 3 below.
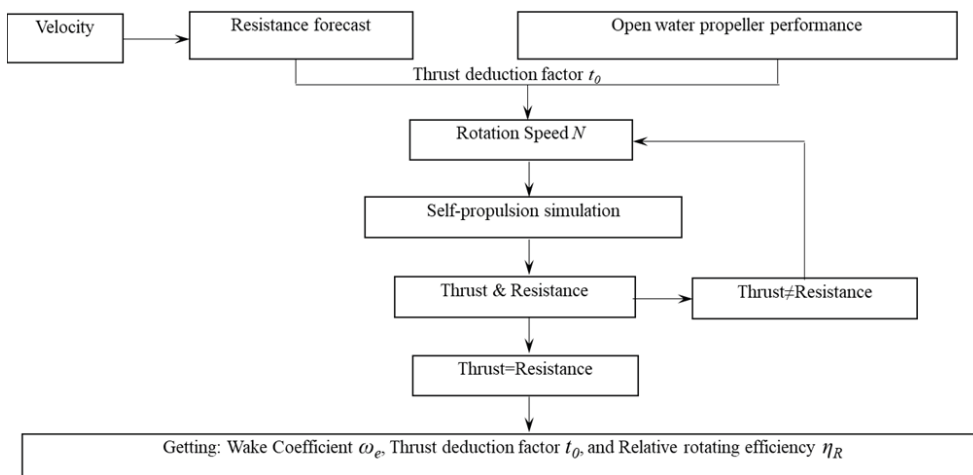

Fig. 3. Determination of the self-propulsion point

SIMULATION OF THE DUCTED PROPELLER IN OPEN WATER TEST

MODEL, GRIDS AND SIMULATION CONDITIONS

In this study, a standard propeller JD7704+Ka4-70 is chosen first to validate the numerical simulation method. The model and the main parameters of the ducted propeller JD7704+Ka4-70 are shown in Fig. 4 and Table 1.
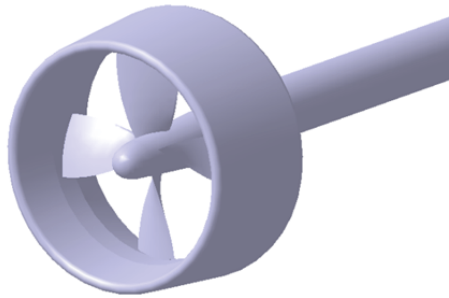

Fig. 4. Model of the standard propeller JD7704+Ka4-70

Tab. 1. Main parameters of JD7704+Ka4-70

Parameters	
Diameter (m)	0.25
Number of blades	4
Gap between blade and duct (mm)	1.5
Revolutions (r/s)	7.5
Reynolds number	4.8×10^5

In order to obtain CFD simulation results with sufficient accuracy, the initial and boundary conditions should be chosen carefully according to the flow problem. Due to the unique structure of the ducted propeller, the diameter of the rotation region should be limited. If the blade tip is too close to the boundary of the rotation region, it will affect the hydrodynamic performance prediction of the propeller, which will lead to a large calculation error. Therefore, in order to accurately predict the hydrodynamic performance of the ducted propeller, the computational domain was divided into three regions: the outermost stationary region, the central rotation region containing the propeller, and the encryption zone of the boundary layer around the duct.

As shown in Fig. 5, the dimensions of the computational domain depend on the characteristic length of the propeller model, which is the diameter of the propeller defined as *D*. The static domain was a cylinder with a diameter of 5*D*. The inlet boundary was located at 2.5*D* ahead of the position of the propeller plane surface. The outlet boundary was set to a length of 5*D* behind the position of the propeller plane. The side of the static domain was defined as symmetry planes. The rotation domain was also a cylinder with a diameter 2 mm larger than the diameter of the propeller and rotated around the X axis at a certain speed. The hydrodynamic

coefficients were predicted by changing the advance speed v_a of the propeller. The transfer of physical quantities between the rotation domain and the static domain is performed via the interface set between the domains.
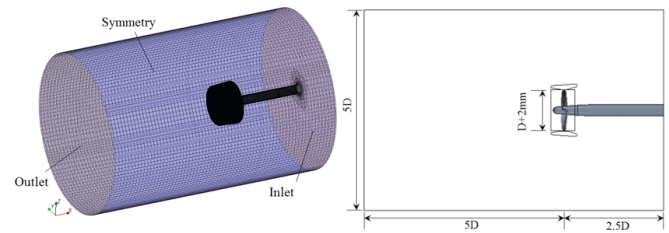

Fig. 5. Computational domain and boundary conditions for JD7704+Ka4-70

Since the gap between the blade and duct is only 1.5 mm, the distance between the outer boundary of the rotation domain and the inner wall of the duct was set to 0.5 mm. The flow at the tip of the blade will become very complicated. So capturing the flow field at the tip of the blade accurately is crucial. Therefore, the mesh of the blade tip area needs to be very refined. The approach is set to a ring-shaped grid encryption zone containing the blade tip gap at the corresponding position, as shown in Fig. 6. The encryption zone needs to exist in both domains at the same time, so that it not only ensures a uniform mesh size on the interface of the two domains, but also guarantees the grid generation of the boundary layer around the duct.
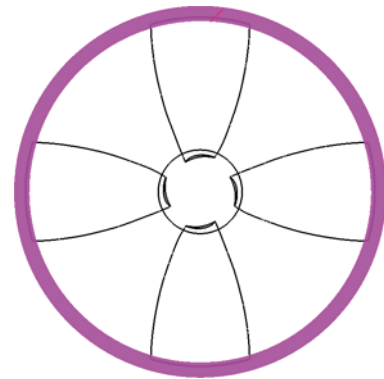

Fig. 6. Grid encryption zone around the blade tip gap

At the same time, the mesh was refined at the leading edge, the trailing edge and the blade. The base size of the grids on the blade and the duct was set to 6‰*D*. It must be ensured that the mesh sizes on the interfaces of the two domains are of the same order of magnitude and as equal as possible so as to be more conducive to the smooth transfer of physical quantities. Moreover, two different sizes of cylinder-shaped grid encryption areas were arranged near the propeller in the static domain to describe the flow field around the propeller, as shown in Fig. 7. It is easily seen that the grids transit smoothly from the blade surface to the static domain.
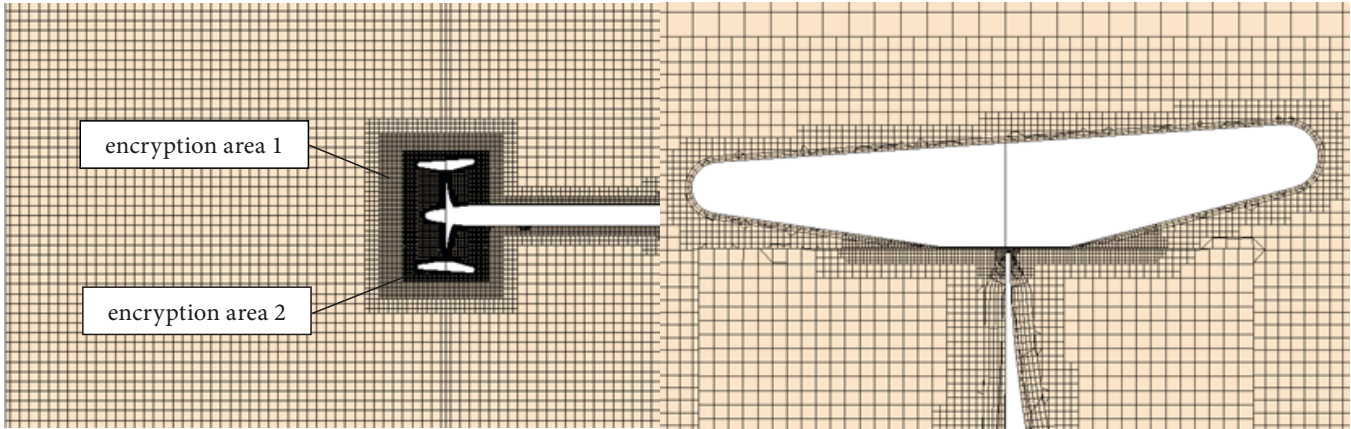
Fig. 7. Refined mesh of the propeller and the interface

The number of grids and nodes are listed in Table 2.

Tab. 2. Grid and node numbers

	Grids	Nodes
Rotation domain	1294307	1697505
Static domain	1625822	2031813
Total	2920129	3729318

Fig. 8 shows the surface grids of the blade and the duct. The grid distribution on the propeller's blade is clearly displayed. The mesh sizes of the blade surface and the mid-leaf area are larger than the grid size of the leading edge and the trailing edge. For the surface mesh of the duct, the size near the blade tip gap is small, and the mesh between two regions transits smoothly.
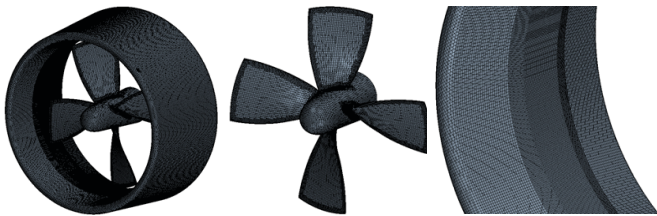
Fig. 8. Blade and duct mesh size

The boundary conditions were given as follows: the inlet was a given uniform flow inlet boundary condition; the outlet was defined as a pressure outlet; the side of the static domain was given as a symmetry plane boundary condition. The coordinate system conformed to the right-hand rule, the origin was set at the centre of the propeller plane surface, and the X axis was set to positive in the opposite direction to the flow.

The initial flow field was calculated using the SM method, then, when the field was fully developed, the MRF method was used alternately, which facilitates the convergence of the calculation [17]. When using the MRF method for steady analysis, the flow can be considered as an absolutely uniform flow without considering the influence of gravity. However,

when using the SM method for unsteady analysis, in order to be able to simulate the rotation under actual conditions, the influence of gravity should be taken into account.
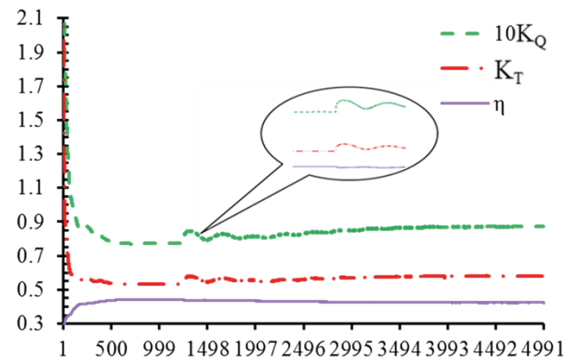
NUMERICAL RESULTS AND ANALYSIS

Fig. 9. Convergence history of the propeller open water curves when J=0.4

Fig. 9 above shows the convergence history of the hydrodynamic coefficients of JD7704+Ka4-70 when J is equal to 0.4. When the method is changed from SM to MRF, there is a small jump in the coefficient curves. Since there is already a fully developed flow field around the propeller before the method is changed, it can quickly stabilise in the subsequent calculation.
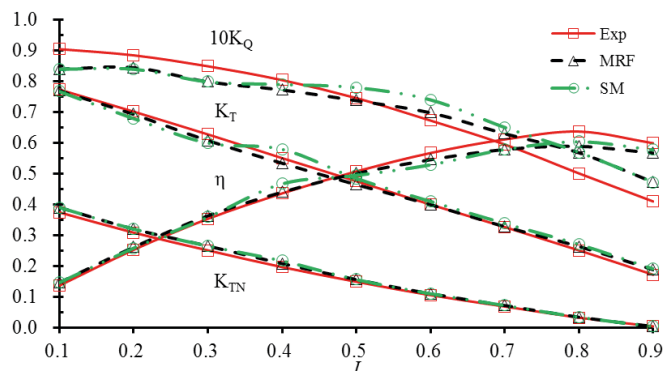

Fig. 10. Open water characteristic curves of JD7704+Ka4-70

As can be seen from Fig. 10 above, in the case of a given uniform flow, the numerical calculation results obtained by using SM for the unsteady method calculation have slightly larger errors than the results obtained by the MRF steady algorithm. Because the test was carried out in a uniform flow, which was a steady situation, it is not necessarily applicable for the unsteady method. It also shows that the SM method requires a higher grid quality than the MRF method. In the case of high advance coefficients, the deviation of the calculated values and test values is larger. And it is worth noting that when J is equal to 0.8 and 0.9, the errors of K_T, K_{TN} and $10K_Q$ obtained by the two methods are large, and all in the range of 10–15%. On the other hand, the error of η does not exceed 6% throughout this process.
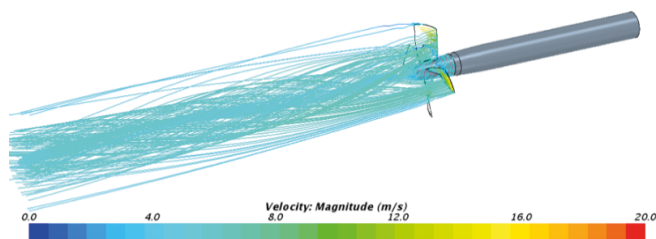

Fig. 11. Wake streamline scalar when J=0.4

Fig. 11 above shows the wake streamline scalar of JD7704+Ka4-70 when J is equal to 0.4. It can be seen that the flow in the field is accelerated to the downstream under the action of the blade. The rectification effect of the duct makes the streamline flowing through the propeller more concentrated, which is the reason why the propulsion efficiency of the ducted propeller is higher than that of the conventional propeller.
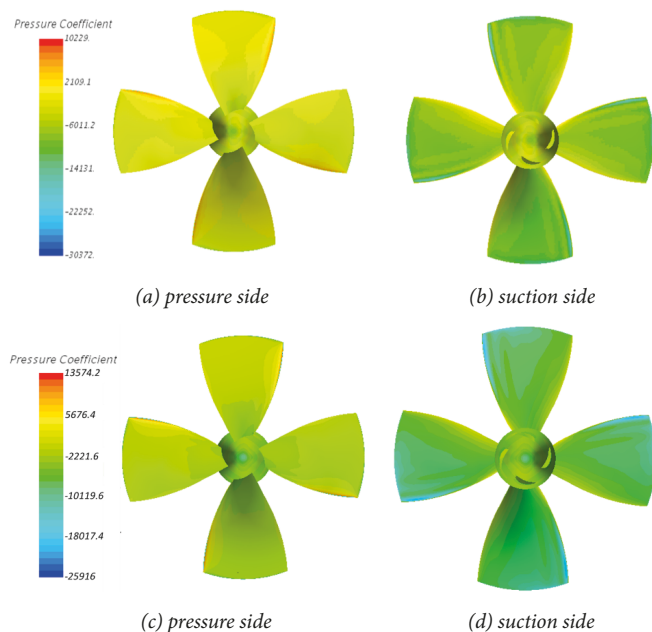

(a) pressure side   (b) suction side

(c) pressure side   (d) suction side

Fig. 12. Pressure distributions on blade when J=0.4: MRF (upper diagram), SM (lower diagram)

As shown in Fig. 12 above, on the pressure side of the propeller, the leading edge is a high pressure zone, which is the main area of the thrust formation. The high velocity in the gap between the blade and duct causes the blade tip and the trailing edge to be the low pressure zone, which is an important feature of the flow field inside the ducted propeller. And on the suction side, there is a wide range of low pressure zone in this area, which is mainly concentrated on the leading edge and the mid-area at the back of the propeller blade. This low pressure zone is not weakened at the blade tip like other conventional propellers, but extends to the inner surface of the duct, as shown in Fig. 13 below.
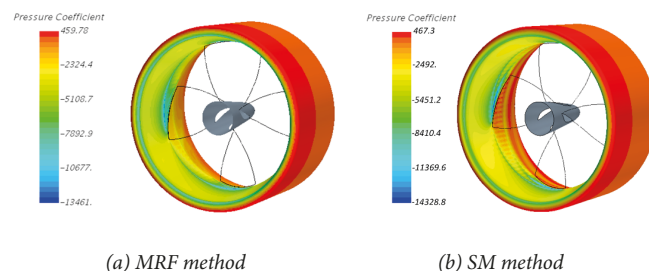

(a) MRF method   (b) SM method

Fig. 13. Pressure distributions on duct when J=0.4

In Fig. 13, there is a low pressure zone at the tip of the blade, which is due to the suction effect on the upstream region caused by the rotation of the propeller. Likewise, the speed of the external flow is much slower than that inside the duct, and the pressure on the outer surface of the duct is larger than that of the inner wall, which is also the cause of the thrust.

SIMULATIONS OF THE DESIGNED DUCTED PROPELLER

MAIN PARAMETERS

According to related references and propeller design handbooks [18], the ducted propeller matched with the USSV is designed based on the standard propeller model JD7704+Ka4-70. Its main parameters are shown below in Table 3.

Tab. 3. Main parameters of the designed ducted propeller

Parameters	
Diameter (mm)	92
Number of blades	4
Gap between blade and duct (mm)	1.5
Reynolds number	5.3×10^5

NUMERICAL RESULTS AND ANALYSIS

For the steady numerical simulation of the designed ducted propeller carried on the USSV, the same grid scheme and boundary conditions as in the previous section were applied,

using the MRF method and with a propeller revolving speed of 68 r/s without considering the influence of gravity. The calculation results are compared with the regression analysis results given in the design manual [18].
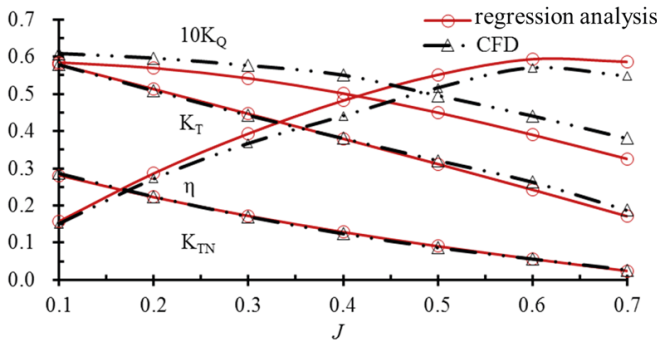

Fig. 14. CFD simulations and regression analysis results

Fig. 14 above shows the CFD steady simulation results compared with regression analysis results when the advance coefficient J is from 0.1 to 0.7. The error of K_T and $10K_Q$ increases gradually with the increase of J. The error of K_T does not exceed 10%, while the error of $10K_Q$ increases obviously. When J is equal to 0.7, the maximum error reaches 16.934%. The changes of η and K_T are relatively small and the maximum error is less than 8.6%.

The hydrodynamic coefficients obtained by the regression analysis are based on the experimental tests and are a polynomial of the propeller pitch and the advance coefficient. The diameter of the test propeller is 250 mm and the gap between the blade and duct is 1.5 mm, while the diameter of the designed ducted propeller used on the USSV is 92 mm with the same gap. The internal flow of the gap is complicated, so there are certain scale effects, which is the main reason for the errors between the CFD simulation results and regression analyses.

It can be seen from Fig. 15 that $Y+ < 200$ when J is from 0.1 to 0.7, and meets the requirements of the solver for the simulation of the flow near the wall using the SST k-ω turbulence model.
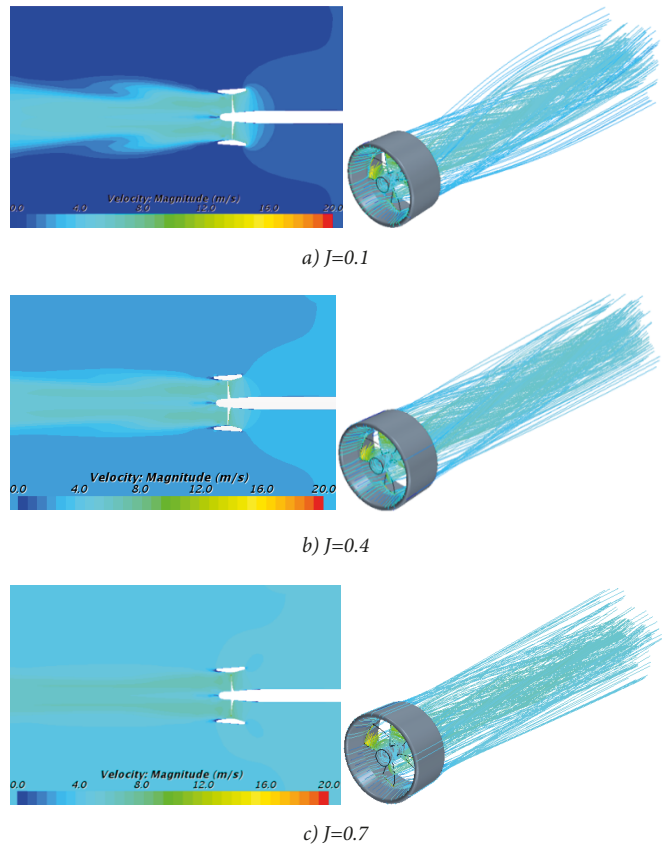

a) J=0.1

b) J=0.4

c) J=0.7

Fig. 16. Velocity distributions and wake streamline scalars of the designed ducted propeller
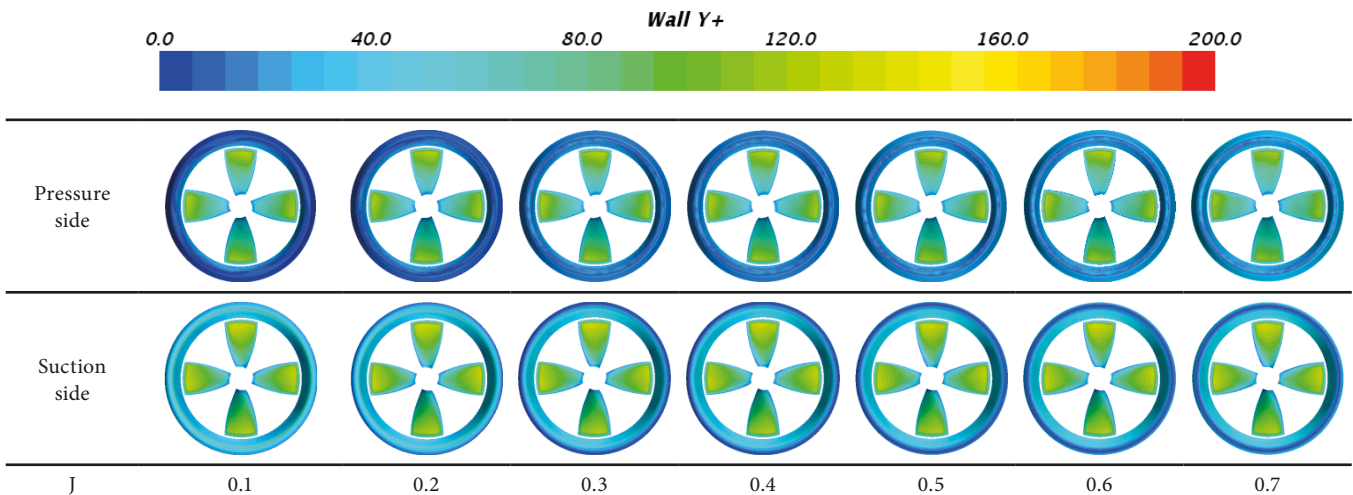

Fig. 15. Wall Y+ distribution of the blade

As can be seen from Fig. 16, the velocity distributions of the flow field in the mid-longitudinal section of the propeller are completely symmetrical with respect to the upper and lower sections along the axis of the shaft, regardless of the influence of gravity. The wake fields of the propeller are relatively regular and smooth, and with the increase of the advance ratios, the rectification effect of the duct on the propeller wake flow is more obvious. The wake flow streamlines are constrained to the cylinder area where the duct is located. So the thrust efficiency also increases.

SIMULATION OF THE SEMI-SUBMERGED VEHICLE SELF-PROPULSION TEST

After performing numerical simulations of the open water test of the USSV-matched ducted propeller, the simulation of the self-propulsion test of the USSV is carried out using a straight-line moving attitude without inclination, and the self-propulsion point is obtained.

MODEL, GRIDS AND SIMULATION CONDITIONS

The model of the USSV with full appendages is shown in Fig. 17 below. The X axis is aligned with the propeller shaft, pointing to the bow of vehicle. The Y axis points from starboard to port and the Z axis points from bottom to top.
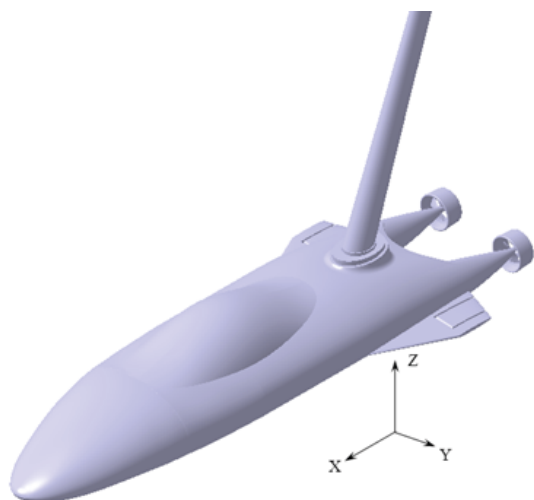

Fig. 17. Model of the USSV with full appendages

The simulation boundary conditions of the USSV self-propulsion test were set as follows: the computational domain was also divided into two different domains, one was a static domain containing the USSV and the other was a rotation domain including the ducted propeller. The left side of the static domain was defined as the pressure outlet and the other boundaries were all set as velocity inlets, given the uniform flow at the corresponding speed. The calculation domain is shown in Fig. 18. The dimensions of the computational domain depend on the characteristic length of the ship model, which is the overall length of the USSV defined as L. The inlet boundary was located $1L$ ahead of the USSV's forward perpendicular, the outlet boundary $3L$ behind the aft perpendicular, and the side boundaries which were also velocity inlet boundaries were $1.5L$ to the mid-longitudinal section of the USSV.
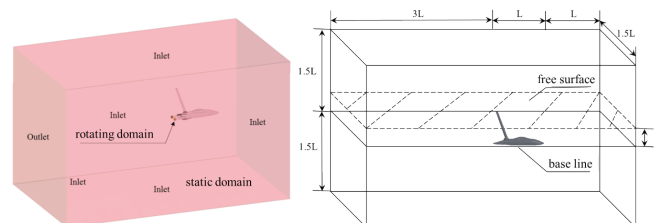

Fig. 18. Computational domain and boundary conditions for self-propulsion test

The calculation condition was chosen as the speed V=5 knots, the draft T=600 mm, and the corresponding resistance of the USSV in calm water can be found in [19]. In the propeller model open water test, when the immersion depth of the propeller shaft is greater than $1.5D$ (D is the diameter of the propeller), the influence of the free surface is negligible [20]. In this section, the shaft immersion depth is $5.67D$, which is much larger than $1.5D$. So the free surface effect on the propeller can be ignored. The numerical grids of the self-propulsion test computation are shown in Fig. 19.
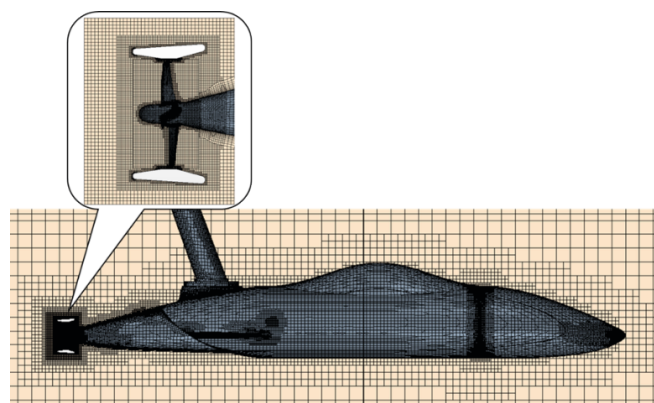

Fig. 19. Numerical grid of self-propulsion test computation

NUMERICAL RESULTS AND ANALYSIS

When the velocity is 5 knots and the draft is 600 mm, the total resistance of the USSV in calm water is 107.5 N. Setting the initial thrust deduction coefficient t_0 equal to 0.11, the maximum efficiency point K_T is 0.2425. At this moment, the initial speed N_0 is 59.015 r/s. It is proposed to determine the self-propulsion point by changing the propeller revolving speed to get the thrust of the propeller and resistance of the USSV in calm water. The free surface waves of the USSV in calm water are shown in Fig. 20.
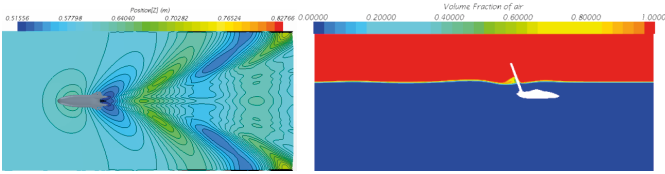
Fig. 20. Free surface waves of the USSV in calm water

It can be seen from Fig. 20 above that, when the USSV sails near the free surface, a series of Kelvin waves are generated on the free surface. At the same time, there is a clear interaction between the free surface and the mast of the USSV. It can be seen from Fig. 20 that there is a significant deformation of the water surface at the position where the mast is in contact with the free surface.

Tab. 4. Thrust and resistance at different rotational velocities

N/rps	V/kn	D/mm	J	Resistance/N	Thrust/N
59.015	5	92	0.4737	78.00	98.59
55.000	5	92	0.5083	76.31	82.41
52.500	5	92	0.5325	75.41	73.05

According to the simulation process shown in Fig. 3, the corresponding thrust and resistance are shown in Table 4 above. In the light of the resistance and total thrust at different advance ratios J, two lines are drawn in Fig. 21 below, where the intersection point is the required self-propulsion point.
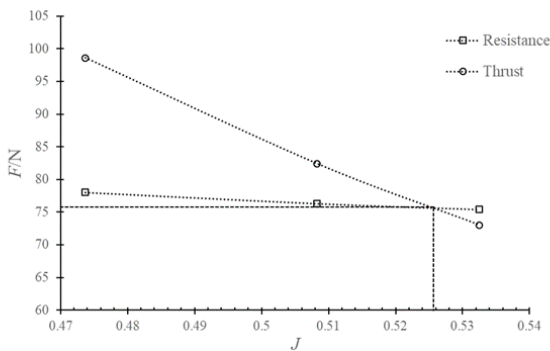

Fig. 21. Self-propulsion point

When the thrust is equal to the resistance, the self-propulsion point is obtained. At this moment, the thrust and the resistance is 75.58 N, the advance coefficient J is 0.5258, and the thrust deduction coefficient t_0 is 0.2888.
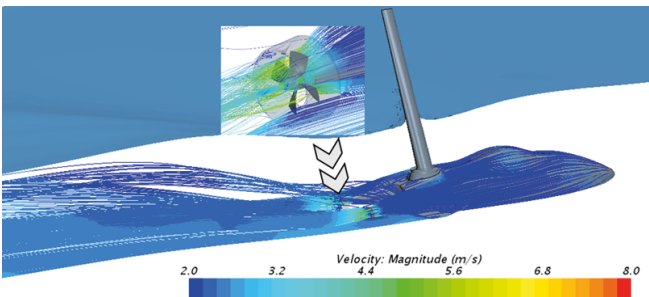

*Fig. 22. Wake streamline scalar of the self-propulsion test*

Fig. 22 shows the shape of the wake flowing through the hull and the propeller when the revolutions of the propeller equal 55 r/s. It can be clearly seen that the suction effect of the upstream fluid by the propeller, and the fluid in front of the propeller is accelerated to the downstream. Compared with the result of the propeller open water simulation, the wake flow is no longer constrained to a cylinder area where the duct is located, but tends to spread out at a certain distance behind the propeller, and the wake flow is partially close to the free surface under the interaction of the hull, appendages and the free surface.
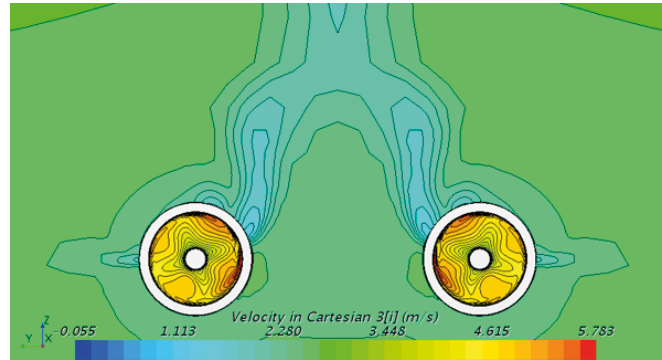
(a) velocity distribution of the propeller at x/D = 0.4 from the propeller plane
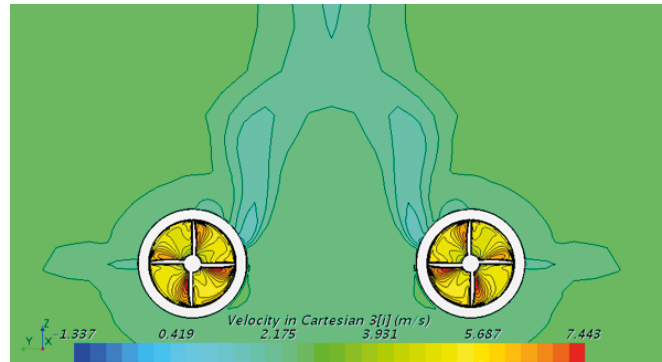
(b) velocity distribution at the propeller plane
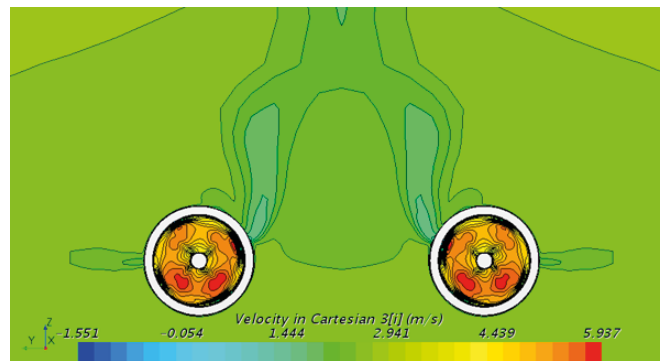
(c) velocity distribution of the propeller at x/D = -0.4 behind the propeller plane

Fig. 23. Velocity distributions at the propeller plane when n=55r/s

Fig. 23 above shows the velocity distributions at three different planes of the ducted propeller. The upper diagram is the upstream velocity distribution at the distance $x/D = 0.4$ from the propeller plane. The middle diagram is the velocity

distribution at the propeller plane. And the lower diagram is the downstream velocity distribution behind the propeller plane at x/D=-0.4. It can be seen from the figure that the fluid flowing through the hull of the USSV causes an inhomogeneity in the flow field in front of the propeller, so the velocity distribution at the propeller plane is also non-axisymmetric, which has a certain negative effect on the propulsion efficiency, and this can also result in increased noise and vibration of the propeller.

CONCLUSIONS

The paper embodies a series of numerical simulations of the propeller open water test and the self-propulsion test of an unmanned semi-submerged vehicle (USSV), using the CFD software Star-CCM+ and the RANS equations combined with the SST k-omega turbulence model. In order to validate the numerical approach, a standard propeller model JD7704+Ka4-70 was used to perform the simulations of an open water test and the CFD results were compared with the experimental results to evaluate the numerical method. The results showed a reasonable agreement, indicating the feasibility and effectiveness of the technique in the simulations.

Afterwards, simulations of a ducted propeller designed based on the standard propeller model JD7704+Ka4-70 were carried out. The ducted propeller was designed to match with the USSV and the open water characteristic curves were obtained. The hydrodynamic coefficients were calculated and the wake streamlines of the ducted propeller were vividly obtained. The reason why the propulsion efficiency of the ducted propeller is much higher than the conventional propeller was gained from the diagram of streamlines.

Finally, a simulation of the self-propulsion test of the USSV with the designed ducted propeller was conducted. The self-propulsion point was obtained by making the resistance equal to the thrust when the velocity was defined as 5 knots and the draft was 600 mm. At this moment, the thrust deduction coefficient t_0 is 0.2888. The wake flow streamlines and the velocity distributions at different propeller planes were also simulated.

However, in the simulation of the self-propulsion test of the USSV, asymmetric velocity distribution at the propeller plane caused increased noise and vibration, thus affecting the propulsion efficiency and reducing the lifespan of the propeller. This adverse impact needs to be addressed in future works.

REFERENCES

1. Savas S., Ali D., Cihad D., Sakir B. (2018): *Investigation of self-propulsion of DARPA Suboff by RANS method*. Ocean Engineering, Vol.150, 258-271.

2. Nathan C., Pablo M. C. (2013): *Submarine propeller computations and application to self-propulsion of DARPA Suboff*. Ocean Engineering, Vol.60, 68-80.

3. Yang C. L., Zhu R. C., Miu G. P., Fan J., Li Y. L. (2011): *CFD-based numerical simulation of hull /propeller /rudder interaction*. Chinese Journal of Hydrodynamics, 26(06), 667-673.

4. Tahara Y., Wilson R. V., Carrica P. M., Stern F. (2006): *RANS simulation of a container ship using a single-phase level-set method with overset grids and the prognosis for extension to a self-propulsion simulator*. Journal of Marine Science and Technology, 11(4), 209-228.

5. Cheng X. K., Zhou Z. Y., Chen K., Wei F. F., Lu C. L. (2013): *Numerical simulation of self-propulsion experiment*. International Journal of Naval Architecture and Ocean Engineering, Issue.03, 10-15.

6. Wu Z. H., Chen Z. G., Dai Y. (2013): *Numerical prediction of self-propulsion with a body-force propeller model*. Journal of Shanghai Jiaotong University, 47(06), 943-949.

7. Carrica P. M., Castro A. M., Stern F. (2010): *Self-propulsion computations using a speed controller and a discretized propeller with dynamic overset grids*. Journal of Marine Science and Technology, 15(4), 316–330.

8. Abbas N., Kornev N., Shevchuk I., Anschau P. (2015): *CFD prediction of unsteady forces on marine propellers caused by the wake non-uniformity and non-stationarity*. Ocean Engineering, Vol.104, 659–672.

9. Ponkratov D., Zegos C. (2015): *Validation of ship scale CFD self-propulsion simulation by the direct comparison with sea trials results*. In: Fourth International Symposium on Marine Propulsors, Austin, Texas, USA, 2015.

10. Yang R. Y., Shen H. C., Yao H. Z. (2005): *Numerical simulation on self-propulsion test of the submarine with guide vanes and calculations for self-propulsion factors*. Journal of Ship Mechanics, 9(02), 31-40.

11. Chase, N. (2012): *Simulations of the DARPA Suboff submarine including self-propulsion with the E1619 propeller*. Master thesis, University of Iowa, USA.

12. Chase N., Carrica P. M. (2013): *Submarine propeller computations and application to self-propulsion of DARPA Suboff*. Ocean Engineering, Vol.60, 68–80.

13. Zhang N., Zhang S. (2014): *Numerical simulation of hull/propeller interaction of submarine in submergence and near surface conditions.* Journal of Hydrodynamics, 26(01), 50–56.

14. Shi Y. X., Zhang L. X., Shao X. M. (2014): *Numerical study of the hydrodynamic performances of surface piercing propeller.* Journal of Mechanical and Electrical Engineering, 31(08), 985-990.

15. Sigmund S., El Moctar, O. (2016): *Numerical prediction of the propulsion characteristics of ships in waves.* In: Proceedings of the International Conference on Offshore Mechanics and Arctic Engineering, Busan, South Korea, 2016.

16. Mehran M. N., Mohammad B., Hassan G., Manouchehr F. (2017): *Numerical analysis of ducted propeller and pumpjet propulsion system using periodic computational domain.* Journal of Marine Science and Technology, 22(3), 559-573.

17. Zhao C. (2014): *Research on CFD simulation method of propeller performance in non-uniform inflow.* Master thesis, Shanghai Jiaotong University, Shanghai, China.

18. Chen K. Y. (2004): *Ship design practical manual.* National Defense Industry Press: Beijing, China

19. Tan G. G. (2017): *Study on the maneuverability of twin tail unmanned semi-submerged vehicle near free surface.* Master thesis, Harbin Engineering University, Harbin, China.

20. Zhang N., Zhang S. L., Shen H. C., Xie H. (2012): *Numerical simulation and verification of free surface craft/paddle interference characteristic.* Chinese Journal of Hydrodynamics, Issue.01, 94-99.

CONTACT WITH THE AUTHORS

Jin Zou
e-mail: zoujin19@126.com

Harbin Engineering University,
Nantong, 150001 Harbin,
China

Guoge Tan
e-mail: tgg_920721@hrbeu.edu.cn

Harbin Engineering University,
Nantong, 150001 Harbin,
China

Hanbing Sun
e-mail: 592415376@qq.com
Harbin Engineering University,
Nantong, 150001 Harbin,
China

Jie Xu
e-mail: 18845142486@163.com
Chongqing Changan Automobile Co., Ltd,
Jianxin, 400000 Chongqing,
China

Yongkang Hou
e-mail: tgg_920721@sina.com
Harbin Engineering University,
Nantong, 150001 Harbin,
China